Available online at www.sciencedirect.com
SCIENCE DIRECT®
Geochimica et Cosmochimica Acta 70 (2006) 1059–1075
Geochimica
www.elsevier.com/locate/gca

Crystallization rates of shock melts in three martian basalts: Experimental simulation with implications for meteoroid dimensions

Erin Walton [a,b,*], Cliff Shaw [b], Steven Cogswell [c], John Spray [a,b]

[a] Planetary and Space Science Centre, University of New Brunswick, Fredericton, New Brunswick E3B 5A3, Canada
[b] Department of Geology, University of New Brunswick, Fredericton, New Brunswick E3B 5A3, Canada
[c] Microscopy and Microanalysis Facility, University of New Brunswick, Fredericton, New Brunswick E3B 5A3, Canada

Received 18 April 2005; accepted in revised form 19 October 2005

Abstract

Dynamic crystallization experiments have been performed on synthetic glasses representative of shock-generated melts observed in Los Angeles, Sayh al Uhaymir 150 and Dar al Gani 476 martian basalts. On the basis of qualitative (texture) and quantitative (fractal analysis) results, we show that melt pockets in Los Angeles cooled at a rate of 1040–1560 °C/h. Sayh al Uhaymir 150 and Dar al Gani 476 melt pockets cooled at 780 °C/h. Conductive cooling models, for a range of meteoroid diameters (10–50 cm), indicate that the minimum meteoroid diameter was small, on the order of 10–15 cm and that melt pockets cooled from post-shock temperatures within minutes. Our results also have bearing on shock implanted martian atmospheric components because it is during cooling that the melt pockets have the potential to lose gases. Modeling of argon diffusion in a spherical melt pocket indicates that during cooling and quench crystallization ~4–60% of trapped martian atmospheric argon may be lost from the melt pocket through diffusive transport.

1. Introduction

Melt pockets occur as subrounded to rounded enclaves of silicate glass and crystals, distributed heterogeneously throughout highly shocked martian meteorites (basalts and peridotites). These pockets, interpreted to be the products of shock melting, formed during the impact event that also launched those meteorites exhibiting evidence for a single shock history (basalts) into space. This interpretation is based on: (1) crosscutting relationships with igneous textures and overprinting by terrestrial alteration (calcite veins, etc.), (2) annealing of mechanical shock defects (planar fractures, mosaicism, etc.) in host rock minerals in direct contact with large (mm-size) melt pockets, (3) the presence of high-pressure mineral polymorphs (stishovite, hollandite, etc.) in some melt pockets (Beck et al., 2004), (4) restriction of melt pockets to those martian meteorites recording mechanical evidence for high bulk shock pressures (~28–45 GPa; Fritz et al., 2003) and their absence in lightly shocked samples (~5–25 GPa; Fritz et al., 2003), and (5) the diagnostic signature (in terms of absolute elemental abundances and isotopic ratios) of the martian atmosphere found in melt pockets of several martian meteorites (Bogard and Johnson, 1983; Garrison and Bogard, 1998). The latter line of evidence relies, in part, on the ability of shock-recovery experiments to demonstrate that hypervelocity impact provides a viable mechanism for implanting a sample of ambient gas in melts produced during shock, without elemental or isotopic fractionation (Bogard and Johnson, 1983; Wiens and Pepin, 1988; Bogard et al., 1989).

The formation mechanism(s) and, in particular, the crystallization conditions for the products of shock melting are not well constrained. This is in part because analogous features have not yet been observed in naturally shocked rocks from terrestrial impact craters, nor in controlled laboratory shock-recovery experiments. However, basement clasts showing petrographic evidence for in situ whole rock

* Corresponding author.
E-mail address: j5rng@unb.ca (E. Walton).

0016-7037/$ - see front matter © 2005 Elsevier Inc. All rights reserved.
doi:10.1016/j.gca.2005.10.033

melting are found in both the Ries and Haughton impact craters (Stöffler et al., 1979; Ostertag et al., 1984; Dressler and Sharpton, 1998). To date, the exact mechanism of formation of melt pockets by in situ melting, either by void collapse or shock wave reflections at grain boundaries, or by injection of extraneous molten material into the host rock, remains unresolved (Stöffler et al., 1986, 1991; Wiens and Pepin, 1988; Bogard et al., 1989; Schmitt, 2000; Beck et al., 2004).

The goal of this study is to constrain the post-shock cooling history of melt pockets observed in martian basalt Los Angeles stone 1 (LA 001) and martian olivine-phyric basalts Dar al Gani (DaG) 476 and Sayh al Uhaymir (SaU) 150. This is also pertinent to understanding the martian atmospheric component trapped in the melt pockets, because the cooling history will affect the retention of atmospheric gases.

Synthetic glasses representative of three melt pockets were subjected to dynamic crystallization at varying cooling rates. The crystal shapes developed in the experiments were compared with those found in the natural melt pockets. The experiments constrain the crystallization conditions of the melt pockets, and together with conductive cooling models can be used to determine the minimum diameter of the meteoroid as ejected from the martian surface. Estimates of the terrestrial pre-atmospheric size of the meteoroid enable direct comparison between the results of this study and previous estimates of the diameter of solid material ejected by hypervelocity impact. The latter estimates are based on the terrestrial crater records (Pohl et al., 1977; Stöffler and Ostertag, 1983), the isotopic composition of martian meteorites (Eugster et al., 2002), mass loss from ablation in Earth's atmosphere (Ceplecha et al., 1993; Bland and Artemieva, 2003), and numerical modeling (Artemieva and Ivanov, 2004).

2. Experimental rationale

2.1. Cooling history

This study is concerned with the shock history beginning with shock compression and melting upon rarefaction. High pressure polymorphs can form during the prolonged phase of pressure release when the shock pressure passes through the stability field of the high pressure phase. If the post-shock temperature is high enough, the melt remains fluid after pressure release and forms a low pressure mineral assemblage. If cooling is rapid, a dendritic crystal shape arises from disequilibrium growth, progressing, with decreasing cooling rate, to compact euhedral mineral shapes typical of near equilibrium crystallization conditions. It is this portion of the meteorite's shock history that this study addresses—the crystallization conditions after shock pressure release.

Experimental studies of silicate melts have shown that, by comparing the shapes of crystals produced experimentally with those in rocks of similar composition, it is possible to deduce the cooling rate and the approximate degree of undercooling ($-\Delta T$) at which crystals nucleate and grow (Donaldson, 1976; Lofgren, 1980; Faure et al., 2003).

2.2. Parameters

In the studied samples, it is assumed that the melt pockets cooled during their ejection from the martian surface. The escape velocity of Mars is 5.0 km/s. Since the mean martian atmospheric scale height (at 210 K) is 10.8 km (Zurek et al., 1992), and ejection velocities are fast (>5.0 km/s), the cooling system has been modeled assuming that the melt pockets cooled while the meteoroid was in space at 210 K (black body temperature of Mars; Zombeck, 1990).

2.3. Constraints on the diameter of the lofted fragments

Current models for ejecting rock fragments during hypervelocity impact favor launch of small fragments, 0.1–50 cm diameter, based on terrestrial impact ejecta dimensions (Pohl et al., 1977; Stöffler and Ostertag, 1983), isotopic compositions of martian meteorites (Eugster et al., 2002), mass loss by ablation in Earth's atmosphere (Ceplecha et al., 1993; Bland and Artemieva, 2003), and numerical modeling of solid particles during launch through the martian atmosphere (Artemieva and Ivanov, 2004).

Studies of naturally shocked rocks from terrestrial impact craters have established that the size of displaced shocked rock fragments is inversely proportional to the shock intensity (Pohl et al., 1977; Stöffler and Ostertag, 1983). Crystalline rock fragments in polymict breccias from the Ries impact structure, Germany, shocked to levels comparable to martian meteorites (30–45 GPa), have diameters of <0.5 m, and are generally within the range 0.1–10 cm.

During measurement of the Kr isotopic composition of martian basalts and peridotites, Eugster et al. (2002) observed effects induced by secondary cosmic rays that are strongly depth dependent. Assuming that the total neutron flux for martian meteorites resulted from exposure to cosmic rays in space, the minimum pre-atmospheric size can be estimated based on the slowing down density for epithermal neutrons (30–300 eV), defined as the number of neutrons per volume and time that were slowed down below a certain energy. Using this method, Eugster et al. (2002) obtained a minimum diameter for the studied martian meteorites (8 in total) in the range 44–50 cm.

Zagami, the largest individual martian meteorite recovered to date, has a total mass of 18 kg. Standard estimates of the mass lost by ablation and fragmentation during transit through the Earth's atmosphere show that a stony object traveling at 18 km/s will lose ~90% of its initial mass (Ceplecha et al., 1993; Bland and Artemieva, 2003). However, this value is strongly dependent on the pre-atmospheric velocity, mass, and trajectory. Dynamic modeling by Gladman (1997) showed that the rocks ejected from

Mars will find their way to Earth on a time scale of a few, to at most a few tens, of Ma. This material possesses an Earth-entry velocity of 13 km/s (the vector sum of the meteoroid's heliocentric velocity and the orbital velocity of the Earth). This would result in a much lower ablation loss of 40–60%, corresponding to only 10–20% of the meteoroid's diameter. For Zagami, this corresponds to a pre-entry radius of ~19 cm (assuming a density of 3.23 g/cm^3 appropriate for a basalt).

Artemieva and Ivanov (2004) present numerical calculations for discrete particle motions through the martian atmosphere within the frame of 3D hydrodynamic modeling. They find that a high-velocity, oblique impact into the martian surface producing an impact crater <3 km (consistent with crater counts for Mars) is capable of accelerating fragments to velocities beyond the martian escape velocity (>5.0 km/s). These rock fragments range in diameter from 0.1 to 75 cm. The smaller-diameter particles (<14 cm) are decelerated through interaction with the martian atmosphere, while 30–50% of the larger fragments could escape Mars.

Following previous estimates for the diameter of solid rock fragments ejected during hypervelocity impact, as outlined above, it is concluded that martian meteorites were probably launched from the martian surface as decimeter-size rock fragments, as opposed to meter-size blocks.

3. Experimental methods

3.1. Starting compositions

The bulk composition of selected melt pockets in each of the meteorites (LA 001, DaG 476, and SaU 150) are given in Table 1. Due to the coarse grain size of the LA 001 meteorite, bulk melt pocket compositions were found to be extremely heterogeneous, reflecting localized melting of host rock minerals (Walton and Spray, 2003). Two compositionally distinct melt pockets from LA 001 were selected, based on the difference between their texture and mineralogy (Figs. 1A and B). Since DaG 476 and SaU 150 are similar in terms of both host rock and melt pocket textures, and compositions only one bulk melt pocket composition was selected as a representative of these two meteorites (Fig. 1C).

Table 1
Bulk composition of melt pockets

wt% oxide	Melt pocket 1		Melt pocket 4		Melt pocket 5	
	Calc	Measured	Calc	Measured	Calc	Measured
SiO_2	45.9	45.1	34.0	33.8	48.8	48.8
TiO_2	0.4	0.3	1.1	1.0	0.2	0.2
Al_2O_3	9.2	9.3	3.4	3.4	5.1	5.0
Cr_2O_3					1.2	1.1
FeO[a]	36.0	35.8	31.0	30.9	16.9	16.9
MnO	0.7	0.7	0.7	0.5	0.1	0.1
MgO	1.4	1.4	0.8	0.8	21.8	21.7
CaO	3.7	3.6	16.5	16.6	4.6	4.7
Na_2O	1.8	1.7	0.5	0.3	0.7	0.6
K_2O	1.9	1.8	0.4	′0.3		
P_2O_5	0.1	0.1	11.5	11.5	0.1	0.1
Total	100.0	99.7	99.9	99.1	99.5	99.2
n	27	50	40	50	50	50

Calc, bulk melt pocket composition calculated by averaging SEM EDS raster scan analyses of natural melt pockets in LA (mp 1 and mp 4) and DaG/SaU (mp 5), measured, bulk melt pocket composition determined from synthetic glasses produced from mixtures of high purity oxides and carbonates; n = number of raster scans averaged to estimate bulk composition.

[a] Total Fe reported as FeO.

The bulk composition of melt pockets was determined by averaging scanning electron microscopy (SEM) energy-dispersive spectrometry (EDS) raster scan analyses from individual melt pockets (see Walton and Spray, 2003 for analytical details). EDS rather than wavelength-dispersive spectrometry was used because of its ability to minimize alkali metal migration, especially in glasses (e.g., Spray and Rae, 1995). Owing to the small size (generally less than a few mm's) and heterogeneity within individual melt pockets (μm-size entrained host rock fragments) there are inherent difficulties in determining the bulk composition of melt pockets using many of the conventional techniques (e.g., XRF, INAA, and RNAA, etc.). These conventional techniques involve crushing up the sample as a whole, requiring separation of the melt pocket from the host rock. This can be achieved by analysis of handpicked glass and crystallite separates from the host rock. However, there is always some degree of contamination owing to entrained host rock fragments within melt pockets. In addition, due to the rarity and value of martian material, raster scan analysis is advantageous because it is non-destructive. The non-destructive nature, mobilization minimization and the ability to selectively raster 'clean' areas of the melt pockets (those that do not contain host rock fragments), make EDS raster scan analysis a viable method for estimating the bulk composition of individual melt pockets. Additional supporting evidence is revealed by the apparent independence of bulk composition and texture. For example, melt pocket 1 and melt pocket 5 both contain olivine crystals with swallowtail morphology, despite the difference between their bulk compositions (Table 2).

Ten grams of synthetic glass, representative of each bulk composition, was produced from mixtures of high purity oxides and carbonates. After weighing and mixing, each sample was decarbonated at 950 °C for 12 h and then fused in air in a Fe-doped Pt crucible at 1600 °C. After the initial fusion, each sample was crushed and re-fused to ensure homogeneity. The resultant glasses were ground to a powder in an agate mortar. The composition of the synthetic glasses was checked by SEM EDS raster scan analysis of polished pellets fused on an iridium strip heater at 1700 °C and quenched in <1 s. The bulk composition of the starting products, compared to those calculated from the natural melt pocket, is given in Table 1.

Use of such homogeneous starting material to represent a shock melt requires the assumption that the melt pockets formed from the cooling of what was initially a superheat-

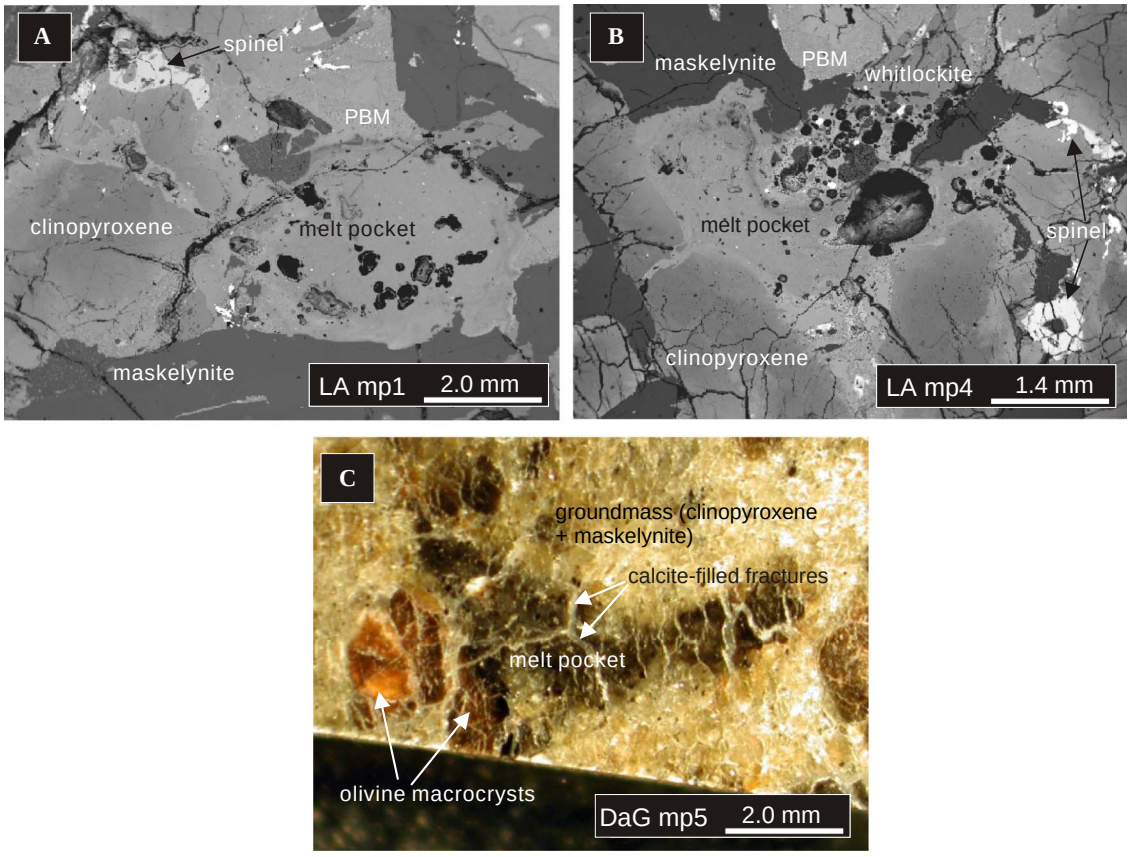

Fig. 1. Photomicrographs showing the natural melt pockets investigated. (A) Melt pocket 1. (B) Melt pocket 4. (C) Melt pocket 5. (A and B) SEM BSE photomicrographs (C) reflected light photomicrograph. PBM, pyroxferroite breakdown material (silica + fayalite + hedenbergite).

Table 2
Results of the error function solution solved for a range of meteoroid diameters (Carslaw and Jaeger, 1959)

	$T_{liquidus}$ (°C)	Meteroid diameter (cm)					
		10	15	25	30	50	100
Melt pocket 1	1200						
t (min)		24	84	310	446	1238	4952
Melt pocket 4	1300						
t (min)		25	117	325	468	1301	5202
Melt pocket 5	1450						
t (min)		30	105	389	560	1554	6218

ed liquid (i.e., liquid free of crystals and crystal nuclei) (Raikhlin et al., 1981; Ivanov and Deutsch, 1999). This may be an over-simplification, since the natural melt pockets contain schlieren that presumably predate the growth of the crystallites, providing nuclei for growth. Two observations are used to justify the method undertaken in this study. First, the mesostasis between dendrite branches and other protuberances is homogeneous and schlieren are generally concentrated near the melt pocket margins, as revealed by back-scattered electron (BSE) observation. Second, one melt pocket observed in DaG 476, does not contain schlieren nor host rock clasts. The olivine crystallites in this melt pocket have the same crystal shape as those observed in schlieren-rich melt pockets in LA 001 and SaU 150. Thus, the crystal shapes observed are not governed by the presence of schlieren. Using this line of evidence we regard the use of homogeneous glasses for starting material suitable for the investigation of melt pocket cooling history.

3.2. Cooling experiments

Cooling experiments were performed on small batches of powder formed into pellets (3–4 mm by ~5 mm), which were then attached to an Fe-doped Pt wire loop at the end of a ceramic rod and suspended in a gas-mixing furnace. Temperature was controlled by a Eurotherm 810 controller. Two separate type R thermocouples were used in each experiment: a control thermocouple attached to the temperature controller and thermocouple built into the oxygen fugacity sensor. The thermocouples were calibrated against the melting points of crystalline diopside (1392 °C) and gold (1064 °C).

Oxygen fugacity was measured by an $SIRO_2$ sensor (from Ceramic Oxide Fabricators) calibrated against the Cu–CuO_2 buffer (Huebner, 1971). Fugacity was controlled and maintained by changing the CO_2 flux via a computer-controlled mass flow controller at constant CO flux. All experiments were performed at 2 log units below the QFM buffer.

For each experiment, the glass-coated wire loop was introduced into the furnace at the starting temperature (T_0) determined for each of the melt pocket compositions, and the fugacity control initiated. After a soak time of 30 min to one hour at this temperature, the samples were cooled over an interval of 208 °C, using the PID controller, at a fixed rate (3120–26 °C/h; Table 3). As the sample was cooled the fO_2 was constantly adjusted by a custom LabVIEW program so that fO_2 was held within ±5% of QFM-2 for the entire run. When the terminal temperature (T_{end}) was reached the gas was switched off and the sample removed from the furnace and quenched in air to room temperature.

Initial liquidus temperature estimates were made using the MELTS software package ($T_{liqMELTS}$; Ghiorso and Sack, 1995; Asimow and Ghiorso, 1998). These estimates were refined using normal quench experiments. The starting temperature (T_0; the temperature at which the pocket is totally molten) was deduced from runs that quenched to a crystal-free glass. For melt pocket composition 1, T_0 was experimentally determined to be 1200 °C. The starting temperature for melt pocket composition 4 was experimentally determined to be 1300 °C and melt pocket 5, 1455 °C.

4. Sample preparation and analysis

After cooling, the samples were vacuum mounted in epoxy. The resultant thick sections were polished to a 0.25 μm finish and carbon-coated in preparation for SEM analysis. BSE images and analyses were obtained using a JEOL 6400 digital SEM with an EDAX Phoenix X-ray microanalysis system equipped with a Sapphire Si(Li) detector and Genesis microanalysis software. SEM analyses were obtained with count times of 60 s, beam conditions of 15 kV and 1.5 nA and a working distance of 14 mm. Analyses were calibrated using a multi-element standard block (Type 202-52) produced by the C.M. Taylor Corporation of Sunnyvale, California. Single spot analyses were

Table 3
Experimental conditions of melt pocket runs

Run No.	Duration (min)	Cooling rate (°C/h)	Texture	T_0 (°C)	Dwell (min)	T_{end} (°C)
Melt pocket 1						
mp1_5	4	3120	Swallowtail olivine	1200	30	992
Oct25a	4	3120	Swallowtail olivine	1200	30	992
Oct25b	4	3120	Swallowtail olivine	1200	60	992
mp1_13	8	1560	Swallowtail olivine	1200	60	992
Oct26a	8	1560	Swallowtail olivine	1200	60	992
mp1_1040	12	1040	Swallowtail olivine	1200	60	992
Oct26b	12	1040	Swallowtail olivine	1200	60	992
mp1_12	16	780	Swallowtail olivine	1200	60	992
Oct26c	16	780	Glass. No crystals present	1200	60	992
mp1_6	20	624	Glass. No crystals present	1200	60	992
Nov1a	30	416	Glass. No crystals present	1200	60	992
Nov1b	40	312	Glass. No crystals present	1200	60	992
mp1_7	60	208	Fine-grained cellular or 'mottled' texture	1200	60	992
Oct25c	60	208	Glass. No crystals present	1200	60	992
mp1_8	129	104	Glass. No crystals present	1200	60	992
mp1_11	240	52	Glass. No crystals present	1200	60	992
mp1_10	480	26	Glass. No crystals present	1200	60	992
Melt pocket 4						
13Nova	4	3120	Fe-oxide dendrites	1300	60	1092
mp1_22	4	3120	Fe-oxide dendrites	1300	60	1092
14Nova	8	1560	Swallowtail apatite, Fe-oxide dendrites	1300	60	1092
15Nova	12	1040	Swallowtail apatite, Fe-oxide dendrites	1300	30	1092
14Novb	16	780	Swallowtail apatite, Fe-oxide dendrites	1300	60	1092
15Novb	20	624	Swallowtail apatite, Fe-oxide dendrites	1300	60	1092
15Novc	30	416	Swallowtail apatite, Fe-oxide dendrites	1300	60	1092
13Novb	60	208	Swallowtail apatite, Fe-oxide dendrites	1300	60	1092
mp1_31	60	208	Swallowtail apatite, Fe-oxide dendrites	1300	60	1092
M4_2 h	120	104	Euhedral apatite	1300	60	1092
M4_4 h	240	52	Euhedral apatite	1300	60	1092
Melt pocket 5						
M5_3120	4	3120	Dendritic olivine and chromite	1455	60	1247
M5_1560	6	1560	Dendritic olivine and chromite	1455	60	1247
M5_1040	12	1040	Dendritic olivine and chromite	1455	60	1247
M5_780	16	780	Dendritic olivine, clinopyroxene and chromite	1455	60	1247
M5_624	20	624	Dendritic olivine, clinopyroxene, euhedral chromite	1455	60	1247
M5_416	30	416	Dendritic olivine, euhedral chromite	1455	60	1247
M5_208	60	208	Dendritic olivine, euhedral chromite	1455	60	1247

used to determine the composition of individual minerals. Raster scans for bulk composition determination were obtained in separate areas of 20 μm × 26 μm.

4.1. Fractal analysis

Fractals are best described as objects that are scale-invariant. This means that they are made up of self-similar components, appearing the same over a large range in scale. Fractal analysis allows quantification of natural objects that, at first observation, may appear to be random or chaotic. Many objects in nature are convex (i.e., a line joining any two points on the perimeter lies within the object), and are bounded by perimeters that are fractal (e.g., coastlines). If a coastline perimeter is measured at a given scale using a set of callipers, the measured perimeter becomes larger as the calliper diameter is reduced. This arises because more of the fine detail of the curve is accommodated. Richardson (see Mandelbrot, 1982) showed a power law relationship between perimeter length and the scale of measurement:

$$\log p = b + m \log a,$$

where b is the constant, a is the caliper aperture, and m is the slope. Mandelbrot (1982) established that the slope defines the fractal dimension, d_f, of an object through the relationship $d_f = (1 - m)$.

There are many natural objects that have a fractal mass distribution, e.g., snowflakes, and, of importance to this study, disequilibrium crystal shapes (e.g., Fowler et al., 1989). Constant density (non-fractal) objects, when measured as a two-dimensional section, scale to the second power of the radius, i.e., the area occupied by the object is proportional to r^2. Objects with a fractal mass distribution scale to a smaller power, the fractal dimension, where $1 < d_f < 2$.

4.1.1. Correlation function

The crystal shape, as viewed in thin section, is a two-dimensional section of a three-dimensional object. Methods for measuring the d_f of two-dimensional sections of fractal objects and curves include the correlation function technique and box methods (Fowler, 1995). In this study, we have implemented the correlation function technique by analyzing crystal shapes using a custom-designed texture correlation calculation (TCC) program, written in Visual Basic at UNB. This enabled quantification of crystal shape in order to compare melt pocket crystals to those crystals formed under controlled conditions in the experiments.

The BSE images of swallowtail and dendritic crystals were converted to binary (black + white) maps. All pixels belonging to the crystal are black and all non-crystal pixels (i.e., those belonging to the mesostasis) are white. BSE images were taken from roughly two orders of magnitude in scale to ensure that information gathered at any given scale is not biased (Fowler, 1995). Ideally, the scaling would be observed over three orders of magnitude on a $\log_{10}$ plot in order for the term "fractal" to be assigned to a crystal shape (Avnir, 1989). However, in our samples (natural and experimental runs), dendritic crystallization is rarely observed at scales greater than a few millimeters. Observation at three orders of magnitude would require TEM sample preparation (nm-scale). Due to the value and rarity of martian materials, the destructive preparation techniques required for TEM observation are undesirable. The scaling range is thus a limitation of the natural and experimental samples (crystal size plus sample preparation) and we regard scaling at two orders of magnitude as satisfactory. Fractal analysis is performed by choosing a black (crystal) pixel as the origin in a series of concentric shells, constructed with increasing radius r (in pixels). Any pixel in the radius circle that is also black counts toward the correlation. The correlation function, $C_{(r)}$, is calculated by dividing the total number of black pixels by the total number of pixels (black + white) in the radius. This gives the probability that a pixel separated from the local origin by distance, r, is part of the crystal. This function has been shown to scale in the same way as the density of pixels in a two-dimensional fractal object (Fowler et al., 1989), i.e., the number of pixels that belongs to the texture is not proportional to the square of r, but to the power d_f, $C_{(r)} = r^{d_f - 2}$. A quantitative value of d_f can be obtained from a double logarithmic density–density plot of $\log C(r)$ versus $\log r$ (Fowler et al., 1989; Fowler, 1995).

Before plotting, the correlation function is scaled to an integer in the range of 0–255. Typically, the raw correlation number would be between 0 and 1 (0 = all white and 1 = all black), however, this program generates a new map as an 8-bit greyscale image. Normalized correlation values, $nC(r)$, thus directly correspond to the grey level in the final image map. This process of selecting a crystal pixel as the origin of a series of subshells is repeated for all black pixels. The data collected for each value of r are then averaged and plotted on a graph of $\log nC_{(r)}$ versus $\log r$. If the analyzed crystal shape is fractal, a straight line relationship with slope $m = d_f - 2$ is obtained. For comparison, an item of constant mass distribution, such as a euhedral phenocryst, would have $m = 0$ hence $d_f = 2$, that of a compact, constant density object (Mandelbrot, 1982).

4.2. Cooling and solidification of melt pockets: conductive cooling model

To estimate the original meteoroid diameter, we consider the case of a non-convecting silicate melt of uniform composition undergoing quenching. Heat loss from the silicate melt is dominated by conduction across a horizontal interface (Carslaw and Jaeger, 1959). The relevant equation for cooling is an error function solution to Fourier's law. The time required for solidification of the melt is calculated for varying distances between the melt pocket and the meteoroid surface (i.e., the depth of the melt pocket within the meteoroid). Initially, the material in the pocket will be at the starting temperature, T_0 (or higher if the melt is

superheated during shock; see Section 3.2). The pocket begins to lose heat to the surrounding material. At some distance from the meteoroid surface the temperature (T) is equal to T_0. This distance increases with time until, eventually, there is no melt left with the temperature T_0 even at the center of the meteoroid. In this event, the boundary conditions have changed and the solution is no longer valid.

For the above scenario, the relevant equation is a special case of Fourier's Law which states that the change in temperature of a substance with time is given by the product of the thermal diffusivity and the derivative of the thermal gradient with respect to distance

$$\frac{\partial T}{\partial t} = \frac{K}{C_p * \rho}\left(\frac{\partial^2 T}{\partial x^2}\right) = k\left(\frac{\partial^2 T}{\partial x^2}\right),$$

where K is the thermal conductivity, C_p is the heat capacity, ρ is the density, k is the thermal diffusivity, and x is the depth of the melt pocket within the meteoroid (one-dimensional heat transfer). The boundary conditions are expressed as:

$$x > 0; \quad T/T_0 \sim 1,$$
$$x < 0; \quad T/T_0 \sim 0.$$

Assuming the thermal diffusivity, k, in the melt and host rock is equal (10^{-6} m^2 s^{-1}), we obtain the solution

$$\frac{T}{T_0} = \frac{1}{2} + \frac{1}{2}\mathrm{erf}\left[\frac{x}{2\sqrt{kt}}\right].$$

This equation can be rearranged to solve the time required for solidification

$$t = \frac{1}{4}\left(\frac{x^2}{k * \mathrm{erf}^2}\right).$$

Using constraints on meteoroid diameter estimates (outlined in Section 2.3), 5 cm was chosen as a lower limit and 50 cm as an upper limit for the distance between the melt pocket and the meteoroid surface (Table 2). Assuming each melt pocket was located at the center of the meteoroid, the diameter is equal to twice the melt pocket depth. Solving the above equation for the three melt pockets for meteoroid diameters of 10, 15, 25, 30, 50, and 100 cm, the time to complete solidification t ranges from minutes at the smallest meteoroid diameters (10–15 cm), to hours at intermediate meteoroid diameters (15–50 cm) and days at the upper limit (100 cm) (Table 2). This calculation does not take into account the latent heat of crystallization.

This is a highly simplified one-dimensional model in which there is a homogeneous temperature gradient from a heat source (melt pocket) to a heat sink (space). In reality, it is probable that the temperature in the host rock was variable. Some areas, like the melt pockets, were strongly heated by shock, others much less so. The cooler portions of the rock would act as the initial primary heat sink for the melt pocket.

5. Results

5.1. Los Angeles

Melt pockets investigated in this study correspond to Type 3 of Walton and Spray (2003), which are differentiated from other melt pocket types on the basis of size, clast volume, and degree of crystallization and vesiculation. These melt pockets are relatively large (>3 mm diameter), vesiculated and are clast-poor, containing flow-textured schlieren and quench crystals.

The first melt pocket investigated in this study (melt pocket 1) contains unzoned olivine neo-crystals embedded in a glassy groundmass. Olivine has swallowtail shapes (see Faure et al., 2003 for nomenclature), and ranges in size from ~15 to 60 μm length and <10 μm width. Olivine crystallites occupy ~55% of the melt pocket by volume. The remaining 45% is divided between ~30% glass and ~15% vesicles.

Melt pocket 4, likewise, is relatively large in apparent diameter (~3 mm × 2.5 mm), but differs from melt pocket 1 in terms of texture and mineralogy. Melt pocket 4 contains unzoned apatite and Fe-oxide neo-crystals embedded in a relatively homogeneous glassy groundmass. Apatite occupies ~38% of the melt pocket by volume, leaving the remaining 62% to Fe-oxides (2%), glass (35%), and vesicles (25%). Apatite crystals are of swallowtail shape and range from 30 to 100 μm in length and 2–12 μm width. Fe-oxides have dendritic (branching) shapes and are finer-grained than the apatite crystals with a branch length of 10–30 μm and branch thickness ⩽1 μm.

5.2. Dar al Gani 476 and Sayh al Uhaymir 150

Large (mm-size) hypocrystalline melt pockets in the olivine-phyric basalts DaG 476 and SaU 150 are essentially identical. A melt pocket was chosen because it shared similar characteristics with the two meteorites, such that the determined cooling rate would be representative for both DaG 476 and SaU 150. This melt pocket, designated melt pocket 5, is almost wholly crystalline, containing olivine (45%) and clinopyroxene (20%) crystals of swallowtail + rod shape, idiomorphic chromite (10%) and interstitial glass (2%). Large melt pockets in the two meteorites are typically highly vesiculated (~23%), a feature quantitatively analyzed by X-ray tomographic techniques in SaU 094 (paired with SaU 150) by Gnos et al. (2002).

5.3. Texture correlation calculation results

An example of the 8-bit greyscale maps generated by the TCC program and the resultant double logarithmic density plot used to determine the fractal dimension is given in Figs. 2 and 3. A summary of the fractal dimension determined for crystals produced in each melt pocket run is given in Table 4. The fractal dimension of natural crystals

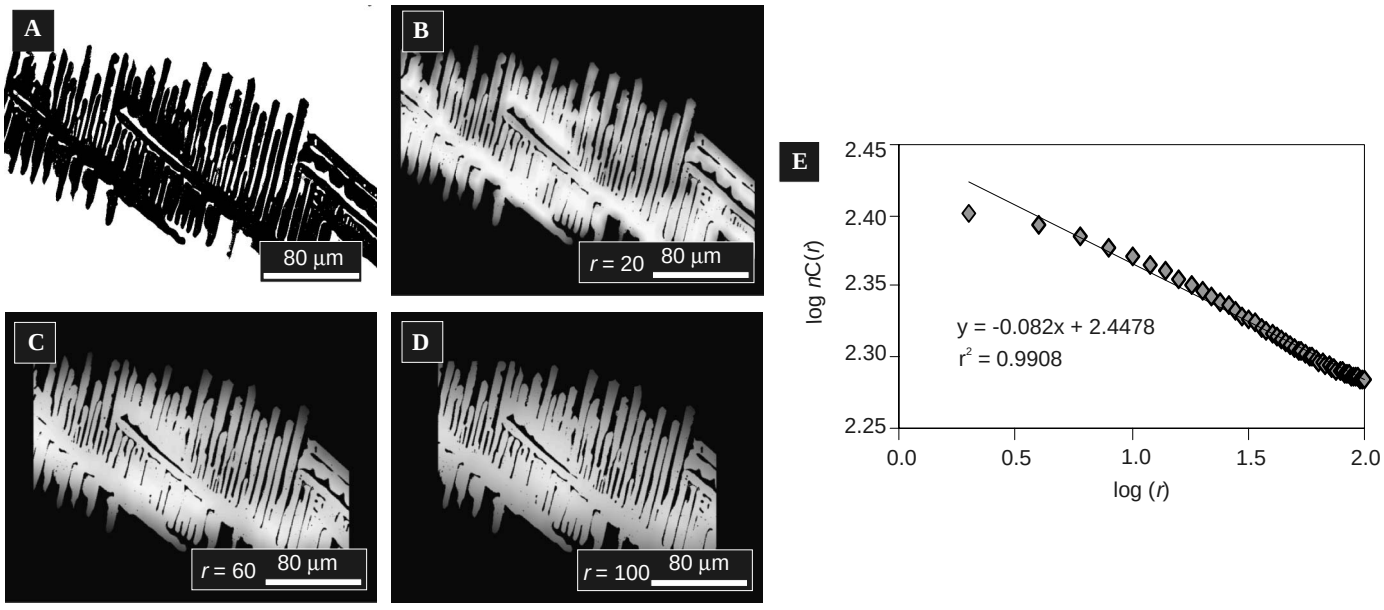

Fig. 2. Texture correlation calculation for apatite observed in an experimental run (melt pocket 4, 13Nova—cooling rate 3120 °C/h). (A) Original binary image. (B–D) The resultant 8-bit greyscale maps produced as radius, r, increases from (B) 20, (C) 60, and (D) 100. Note that with increasing r the decrease in texture correlation is shown as a change in greyscale (white to grey). (E) After the raw data are processed the fractal dimension is determined from log–log plots of r versus the normalized texture correlation $n\mathrm{C}(r)$, where 2 + slope = fractal dimension = 1.918 ± 0.1.

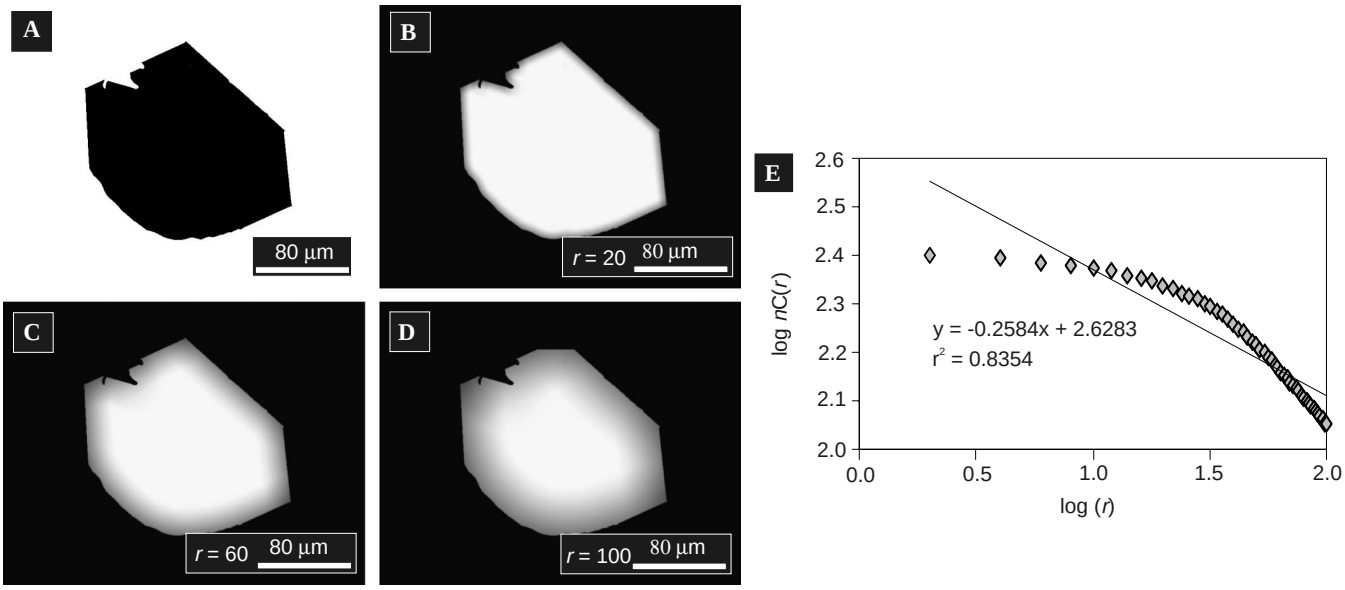

Fig. 3. Texture correlation calculation for apatite observed in an experimental run (melt pocket 4, 2 h–104 °C/h). (A) Original binary image. (B–D) Resultant 8-bit greyscale maps generated by the TCC program showing r increasing from (B) $r = 20$, (E) $r = 60$, and (D) $r = 100$. (E) Graph log $n\mathrm{C}(r)$ versus log r. A straight line relationship is not observed and the crystal shape is no longer that of a fractal object, but has a more compact density distribution.

occurring in the melt pockets of LA 001, DaG 476, and SaU 150 have been measured for comparison (Table 4).

All analyzed olivine shapes in the experimental charges using melt pocket 1 fall on a straight line ($r^2 = 0.9801$–0.9941) with negative slope, confirming their fractal nature (Fowler et al., 1989; Fowler, 1995). Crystals grown at the fastest cooling rates (3120 °C/h) have the highest fractal dimension, in the range 1.7278–1.7482. As the cooling rate decreases from 1560 to 780 °C/h, the fractal dimension decreases from 1.6546 to 1.3470.

Experiments on melt pocket 4 produced Fe-oxide crystals that are fractal ($r^2 = 0.9804$–0.9961) over the entire cooling range (3120–208 °C/h). At the lowest cooling rates (>2 h duration), no Fe-oxides grew from the melt. Apatite crystals are fractal over 1560–780 °C/h. At cooling rates slower than 624 °C/h the d_f and r^2 for apatite decreases from 1.7018 to

Table 4
Fractal dimensions for minerals analyzed in selected martian meteorites and experimental runs

Melt pocket 1	Fractal dimension olivine	r^2				
Los Angeles	**1.7841**	**0.9882**				
mp1_5*	1.7278	0.9892				
Oct25a**	1.7482	0.9941				
Oct25b	1.7258	0.9856				
mp1_13	1.6546	0.9806				
Oct26a	1.6418	0.9879				
mp1_1040	1.6060	0.9801				
Oct26b	1.5394	0.9886				
mp1_12	1.3470	0.9910				
Melt pocket 4	Fractal dimension apatite	r^2	Fractal dimension Fe-Ti oxide	r^2		
Los Angeles	**1.8486**	**0.9884**	**1.4939**	**0.9890**		
13Nova	—	—	1.7018	0.9909		
mp1_22	—	—	1.7213	0.9921		
14Nova	1.9180	0.9908	1.5355	0.9949		
15Nova	1.7654	0.9837	1.6096	0.9925		
14Novb	1.7717	0.9808	1.5325	0.9804		
15Novb	1.8020	0.9722	1.3463	0.9937		
15Novc	1.7726	0.9126	1.4147	0.9878		
13Novb	1.7530	0.9482	1.3471	0.9901		
mp1_31	1.8869	0.9429	1.3337	0.9933		
M4_2 h	Not fractal	0.8078	—	—		
M4_4 h	Not fractal	0.8058	—	—		
Melt pocket 5	Fractal dimension olivine	r^2	Fractal dimension chromite	r^2	Fractal dimension clinopyroxene	r^2
SaU 150	**1.8684**	**0.9947**	Not fractal	—	**1.9204**	**0.9902**
DaG 476	**1.8192**	**0.9846**	Not fractal	—	**1.8607**	**0.9779**
M5_3120	1.7657	0.9871	1.6825	0.9799	—	—
M5_1560	1.7898	0.9862	1.7075	0.9891	—	—
M5_1040	1.8067	0.9874	1.5267	0.9882	—	—
M5_780	1.7824	0.9834	1.6189	0.9882	1.6814	0.9813
M5_624	1.7010	0.9839	1.6319	0.9734	1.3466	0.9923
M5_416	Not fractal	0.8904	Not fractal	0.8731	—	—
M5_208	1.5355	0.9949	Not fractal	0.8267	—	—

—, not applicable (mineral not in run).

1.3955 and 0.9722 to 0.9429, respectively, indicating that the crystals show less fractal behavior with longer cooling duration. At the slowest cooling rates (104 and 52 °C/h) the data points do not fall on a straight line and the crystal shapes have a more compact density distribution.

Olivine, chromite, and clinopyroxene crystals in the experiments on melt pocket 5 are similar to those observed in melt pocket 4. They are fractal at the fastest cooling rates (3120–624 °C/h) and have a compact density distribution at the slowest cooling rates (416 and 208 °C/h). In general, their fractal dimensions decrease with cooling rate.

6. Discussion

6.1. Constraints on cooling rate

Qualitative cooling rate estimates are based on textural and mineralogical similarities between natural melt pockets and experiments. Textural comparisons can be found in Fig. 4 (LA 001) and Fig. 5 (DaG/SaU). Mineral compositions are given in Tables 5–7.

Quantitative cooling rate estimates are based on the fractal analysis of melt pocket crystal shapes (natural melt pocket crystals versus experimental runs). Crystals having similar shapes (swallowtail and dendritic) are produced over a range of cooling rates. For example, in melt pocket 4, swallowtail apatite appears in runs cooled between 3120 and 208 °C/h. Although the slight changes in crystal shape are recognized at an empirical level (from crystals formed at 3120 °C/h compared with crystals formed at 208 °C/h), this is difficult to describe and is observer-specific. For example, what one person describes as a highly branching shape might be highly dendritic, swallowtail dendritic etc. to another observer. How does one describe a crystal that is less highly branching? Are they called medium-branching, less highly branching or slightly dendritic? Clearly, the fractal dimension provides a more quantitative index of crystallinity.

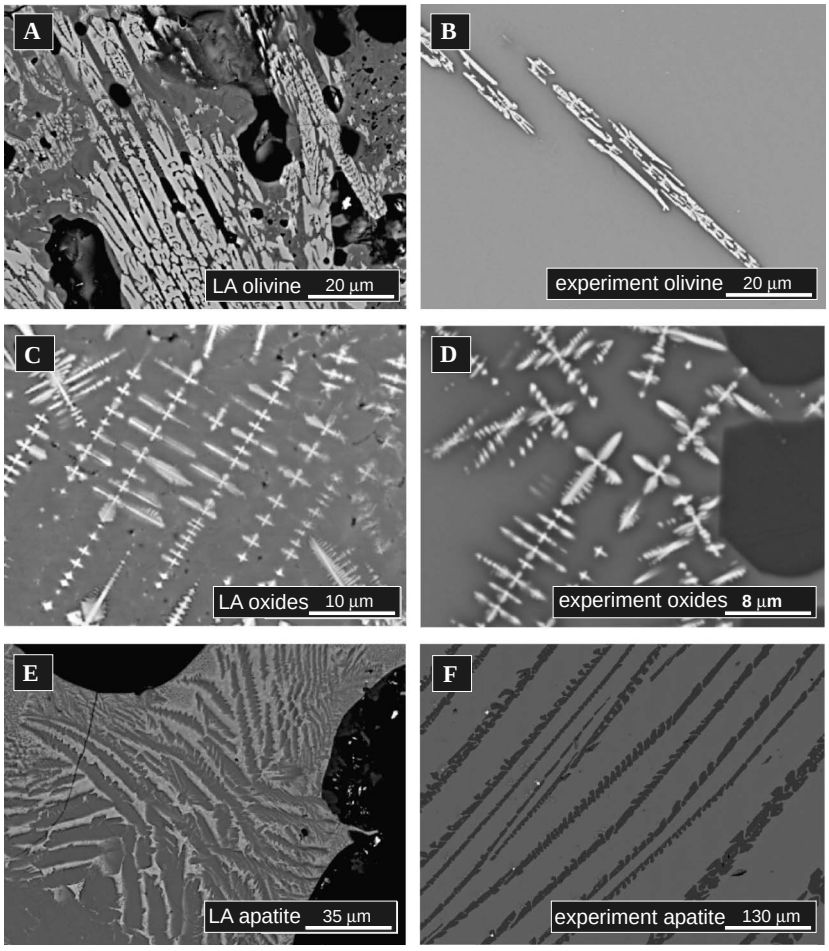

Fig. 4. SEM BSE photomicrographs comparing textures between natural melt pockets in the Los Angeles meteorite (A, C, and E) with crystals formed under controlled conditions in experimental runs (B, D, and F). (B) Melt pocket 1 cooling rate 3120 °C/h. (D) Melt pocket 4 1560 °C/h. (F) Melt pocket 4 780 °C/h. LA, Los Angeles. Experiment refers to crystals observed in dynamic crystallization experiments.

6.1.1. Los Angeles

Two melt pockets from the LA 001 meteorite have been investigated to constrain the post-shock cooling history. The investigation of two melt pockets in a single meteorite provides good internal control on the experiments because melt pockets located within centimeters of each other in the meteorite groundmass are expected to have experienced the same cooling conditions.

Olivine crystals, identical to those observed in LA 001, were grown under cooling rates ranging from 3120 to 780 °C/h. At a cooling rate slower than 780 °C/h olivine crystals ceased to nucleate and grow from the melt and the runs consisted entirely of glass. This observation, crystallization at the fastest cooling rates and formation of a crystal-free glass at the slowest cooling rates, has been observed for all three melt pocket compositions. This can be interpreted in terms of the amount of undercooling as a function of time and the critical radius for nuclei. The critical radius for nuclei at fast cooling rates is small compared to that of a slowly cooled melt where the nucleation rate is low but the growth rate is rapid.

The composition of olivine crystals analyzed in LA 001 melt pocket 1 are Fe-rich ($Fa_{91.8–96.3}$) and overlap with those grown in the experiments ($Fa_{86.9–96.3}$). However, compositional data do not allow refinement of the cooling rate estimates since mineral compositions are constant regardless of cooling rate (Table 5). Likewise, apatite compositions show a good fit between those analyzed from the natural melt pockets and those grown experimentally in terms of wt% oxides for major elements FeO, CaO, and P_2O_5 (Table 6). The fine-grained nature of Fe-oxides made quantitative analysis difficult. Analyses likely include contamination from surrounding glasses (Table 6). Fe-oxides grown in the experimental runs are more Fe-rich and Ti-poor compared with crystals analyzed from the natural melt pockets in LA 001 (Table 6).

The crystals grown far from equilibrium (faster cooling rates) have higher fractal dimensions compared to crystals cooled at slower rates (Table 4). This is observed empirically as a transition from a fractal object (swallowtail and dendritic shapes; Figs. 6A, C, and E; 7A and C) to objects having a more compact density distribution (Figs. 6B, D, and F; 7B and D). Combining fractal dimension data with the qualitative results indicates that melt pocket 1 cooled at a rate of 1040–3120 °C/h (duration of 4–12 min). Melt

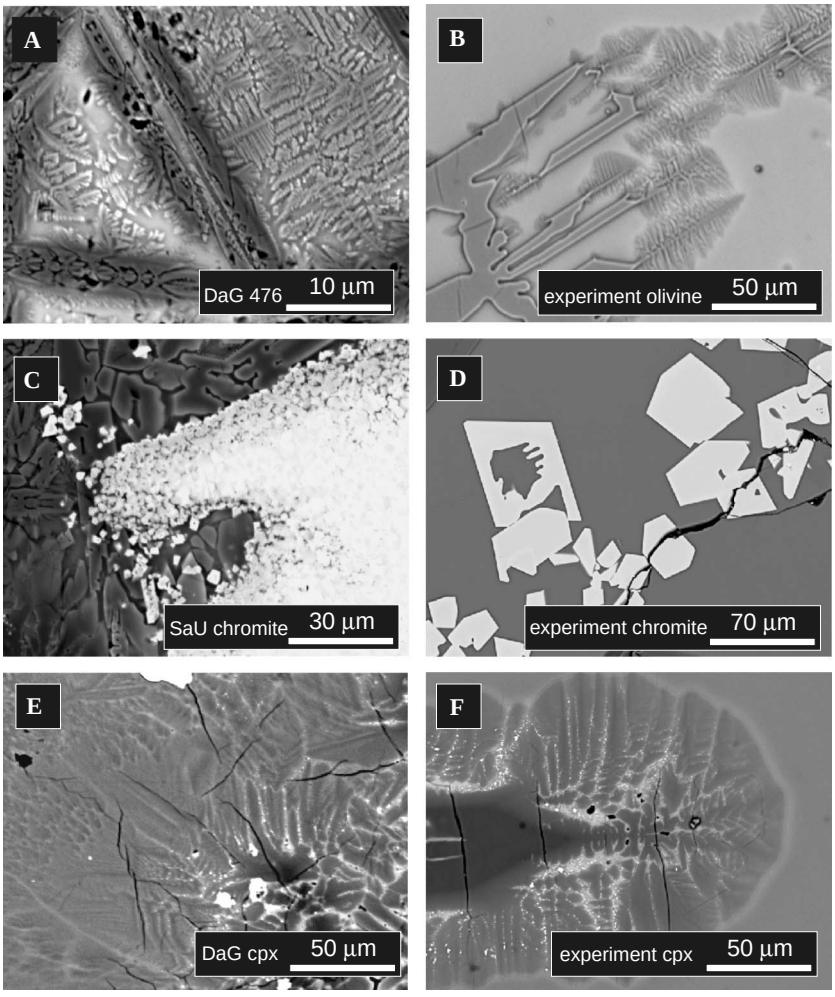

Fig. 5. SEM BSE photomicrographs comparing textures of natural melt pockets in SaU 150 and DaG 476 (A, C, and E) with those observed in melt pocket 5 (B, D, and F). (B) Olivine dendrites formed at a cooling rate of 1040 °C/h. (D) Chromite crystals formed at a cooling rate of 624 °C/h. (F) Clinopyroxene crystals formed at a cooling rate of 624 °C/h. Experiment refers to crystals observed in dynamic crystallization experiments.

Table 5
Representative analyses of olivine crystals in Los Angeles and experiment runs

Melt Pocket 1 olivine	LA olivine meteorite	Experiment								
		mp1_5	Oct 25a	Oct 25b	mp1_13	Oct 26a	mp1_1040	mp1_10	Oct 26b	mp1_12
SiO_2	29.6	31.2	31.7	31.1	29.4	29.9	29.4	29.5	30.6	30.0
Al_2O_3	0.1	0.4	0.8	0.7	0.5	0.4	0.2	0.2	0.5	0.4
Cr_2O_3	b.d.	b.d.	0.0	0.1	b.d.	b.d.	0.1	0.1	0.2	b.d.
FeO	64.3	64.2	63.5	63.2	65.4	63.7	66.1	66.0	63.5	64.6
MnO	1.3	0.6	0.6	0.3	0.7	0.7	0.9	0.8	0.9	0.9
MgO	3.2	3.8	3.0	4.1	3.2	4.8	2.9	2.7	4.0	3.5
CaO	1.2	0.4	0.3	0.2	0.4	0.3	0.1	0.1	0.3	0.3
Na_2O	0.3	b.d.	b.d.	0.1	0.2	b.d.	0.2	0.1	b.d.	0.1
Total	100.0	100.7	99.9	100.1	99.8	99.8	99.9	99.5	100.0	99.8
Fa	91.8–96.3	90.3–90.6	91.4–92.2	89.6–90.6	89.6–92.2	87.9–88.3	92.7	93.2–93.8	89.9–90.0	90.9–91.2

All data reported as wt% oxides. Experiment, crystals observed in experimental charges at varying cooling rates. b.d., below detection limits.

pocket 4 shows a similar range, cooling in the interval 624–1560 °C/h (duration 8–20 min).

6.1.2. Dar al Gani 476 and Sayh al Uhaymir 150

Olivine + clinopyroxene + chromite assemblages, observed in natural melt pockets of DaG 476 and SaU 150 meteorites, were produced experimentally at a cooling rate of 780–624 °C/h (duration of 16–20 min). At cooling rates faster than 780 °C/h (in the range 3120–1040 °C/h) and at cooling rates slower than 624 °C/h clinopyroxene was absent in the experiments. Mineral compositions show a good fit between meteorite crystals and the runs (Table 7).

Table 6
Representative analyses of crystal compositions for melt pocket 4

Melt pocket 4 phosphate	LA meteorite	13 Novb exp	14 Nova exp	14 Novb exp	15 Nova exp	15 Novb exp	15 Novc exp	4 h exp	2 h exp
SiO_2	0.7	0.7	1.3	0.7	0.7	0.8	0.7	0.7	0.7
Al_2O_3	b.d.	0.1	0.1	b.d.	b.d.	b.d.	b.d.	0.1	0.2
FeO	5.7	4.9	5.7	5.3	5.4	5.2	5.6	5.3	5.4
MnO	b.d.	b.d.	0.2	0.1	0.1	0.1	0.2	b.d.	0.2
MgO	0.7	1.0	1.0	1.0	1.0	0.9	0.9	1.1	1.1
CaO	47.1	48.5	48.0	48.5	48.6	48.6	48.7	48.5	48.2
Na_2O	0.6	0.2	0.2	0.2	0.3	0.2	0.2	b.d.	0.1
P_2O_5	44.6	44.4	43.4	44.7	44.2	44.0	43.9	43.2	44.2
Total	99.5	99.9	100.0	100.5	100.3	99.8	100.3	99.1	100.4

Melt pocket 4 oxides + glass	LA Fe-oxide meteorite	13 Novb exp		14 Nova exp		14 Novb exp		15 Nova exp		15 Novb exp		15 Novc exp	
		Fe-oxide	Glass	Fe-oxide	Glass	Fe-oxide	Glass	Fe-oxide	Glass	Fe-oxide	Glass	Fe-oxide	Glass
SiO_2	3.8	6.9	28.6	5.9	27.9	4.5	28.9	10.8	28.0	10.4	28.6	13.0	29.6
TiO_2	23.2	2.7	0.9	4.4	1.1	5.1	1.7	2.2	0.9	3.7	1.1	3.2	1.0
Al_2O_3	1.0	2.4	2.2	2.9	2.6	2.5	5.0	2.1	2.4	1.9	2.5	2.0	2.4
Cr_2O_3	b.d.	b.d.	b.d.	0.3	0.3	0.1	b.d.	0.1	0.1	b.d.	0.2	0.1	0.1
FeO	69.9	78.8	45.4	81.7	47.1	83.9	36.2	73.2	45.4	77.6	44.5	70.3	46.3
MnO	0.4	0.2	0.6	0.2	0.5	0.2	0.2	0.4	0.6	0.1	0.6	0.3	0.6
MgO	0.7	0.6	0.7	0.4	0.7	0.4	0.2	0.4	0.8	0.2	0.6	0.4	0.7
CaO	0.2	4.8	16.1	1.3	15.2	1.3	21.5	6.8	15.7	4.6	16.2	7.5	15.2
Na_2O	n.a.	0.1	0.2	0.1	0.2	0.1	0.4	0.1	0.3	b.d.	0.2	0.1	0.3
P_2O_5	n.a.	2.8	4.7	0.2	4.1	0.2	5.6	2.3	5.0	1.0	5.0	1.9	3.2
Total	99.2	99.3	99.5	98.4	99.7	99.3	99.7	98.4	99.2	99.5	99.5	98.8	99.4

All data reported as wt% oxides. Exp, crystals observed in experimental charges at varying cooling rates. b.d., below detection limits.

Table 7
Representative analyses of melt pocket crystals

Melt Pocket 5	**SaU 150 meteorite**	**DaG 476 meteorite**	M5_3120 experiment	M5_1560 experiment	M5_1040 experiment	M5_780 experiment	M5_624 experiment	M5_416 experiment	M5_208 experiment
Olivine									
SiO_2	37.0	35.9	34.7	37.5	35.4	36.5	36.8	36.2	36.8
Al_2O_3	b.d.	0.3	0.3	1.3	0.2	0.3	0.2	0.2	0.3
Cr_2O_3	0.2	b.d.	0.2	0.4	0.7	0.3	0.7	0.6	0.4
FeO	23.1	28.7	40.2	33.0	28.0	31.8	25.7	28.3	28.1
MnO	0.4	0.5	b.d.	b.d.	b.d.	b.d.	b.d.	b.d.	b.d.
MgO	38.1	33.1	24.2	26.3	34.9	30.3	35.0	33.5	32.9
CaO	0.1	0.2	0.3	0.7	0.2	0.3	0.2	0.2	0.3
Na_2O	0.2	0.4	0.3	0.3	0.3	b.d.	b.d.	0.2	0.2
Total	99.1	99.1	100.2	99.5	99.7	99.5	98.7	99.2	99.0
Fa	22.4–48.2	27.6–40.7	28.4–51.2	30.0–41.3	28.0–33.4	31.0–37.1	28.6–39.0	30.9–32.2	27.8–32.3
Chromite									
SiO_2	0.7	0.5	0.7	0.4	0.6	0.5	0.6	0.2	0.6
TiO_2	0.8	0.8	0.7	0.6	0.9	0.8	0.4	0.8	0.4
Al_2O_3	7.1	7.3	7.4	6.6	6.2	6.5	6.5	6.6	6.3
Cr_2O_3	58.1	57.8	58.2	56.3	56.7	57.9	57.8	57.2	59.7
FeO	28.1	27.6	27.4	28.9	28.9	27.9	26.7	27.8	25.4
MnO	0.4	0.5	0.2	0.2	b.d.	b.d.	b.d.	0.1	b.d.
MgO	3.7	5.0	6.0	6.0	5.7	6.0	7.1	6.7	6.6
Total	99.2	99.5	100.6	99.3	99.2	99.6	99.4	99.4	99.2
Clinopyroxene									
SiO_2	52.0	54.8				49.7	50.7		
TiO_2	0.2	0.2				b.d.	2.5		
Al_2O_3	2.2	0.7				3.5	0.1		
Cr_2O_3	1.0	0.6				2.2	0.2		
FeO	14.6	13.9				16.7	18.1		
MnO	b.d.	0.4				b.d.	0.1		
MgO	25.1	26.6				24.2	23.8		
CaO	4.1	1.5				3.6	3.9		
Na_2O	0.3	0.3				0.2	0.3		
Total	99.5	99.2				100.1	99.7		
En	63.9–74.6	69.3–80.3				64.4–64.8	55.6–61.5		
Fs	17.9–25.6	16.9–24.5				27.7–28.2	30.2–37.8		
Wo	6.8–9.1	2.9–6.2				7.4–7.6	6.5–8.3		

All data reported as wt% oxides; b.d., below detection limits; experiment, crystals observed in experimental charges at varying cooling rates.

Olivine compositions in the natural melt pockets (DaG $Fa_{27.6–40.7}$; SaU $Fa_{22.4–48.2}$) overlap with olivine grown experimentally ($Fa_{27.8–51.2}$). Chromite also shows a good fit between those analyzed from the natural melt pocket and those grown experimentally, particularly for Cr_2O_3, Al_2O_3, and FeO (Table 7). Likewise, clinopyroxene compositions analyzed from natural melt pockets and crystals grown in the experimental runs overlap (DaG $En_{69.3–80.3}Fs_{16.9–24.5}Wo_{2.9–6.2}$; SaU $En_{63.9–74.6}Fs_{17.9–25.6}Wo_{6.8–9.1}$; experimental runs $En_{55.6–64.8}Fs_{27.7–37.8}Wo_{6.5–8.3}$) (Table 7). Based on mineralogy and texture alone the cooling rate can be constrained between 780 and 624 °C/h.

Quantitative fractal dimension analyses show general trends in common with those observed in melt pockets 1 and 4 (see Section 4.1.1). With faster cooling rate d_f decreases, observed for apatite, chromite, and clinopyroxene dendrites. At a cooling rate of 416 °C/h, double logarithmic density plots for apatite and chromite do not fall on a straight line, indicating that the crystals are no longer fractal objects (Fig. 3). This is observed as a transition from swallowtail and dendritic shapes to more compact (euhedral) shapes (Fig. 7). Combining qualitative and quantitative cooling rate estimates melt pocket 5 cooled at 780 °C/h (duration 16 min).

6.2. Cooling rate summary

The datasets do not show systematic variation between mineral composition and cooling rate, therefore, this parameter did not contribute directly to cooling rate estimates. However, the observation that the mineral composition of natural crystals in the melt pockets and experimental runs overlap indicates a good fit for this data. The main qualitative parameters are texture and mineral assemblage. In this study, we have defined fractal dimension results falling within $d_f \pm 0.2$ of the natural

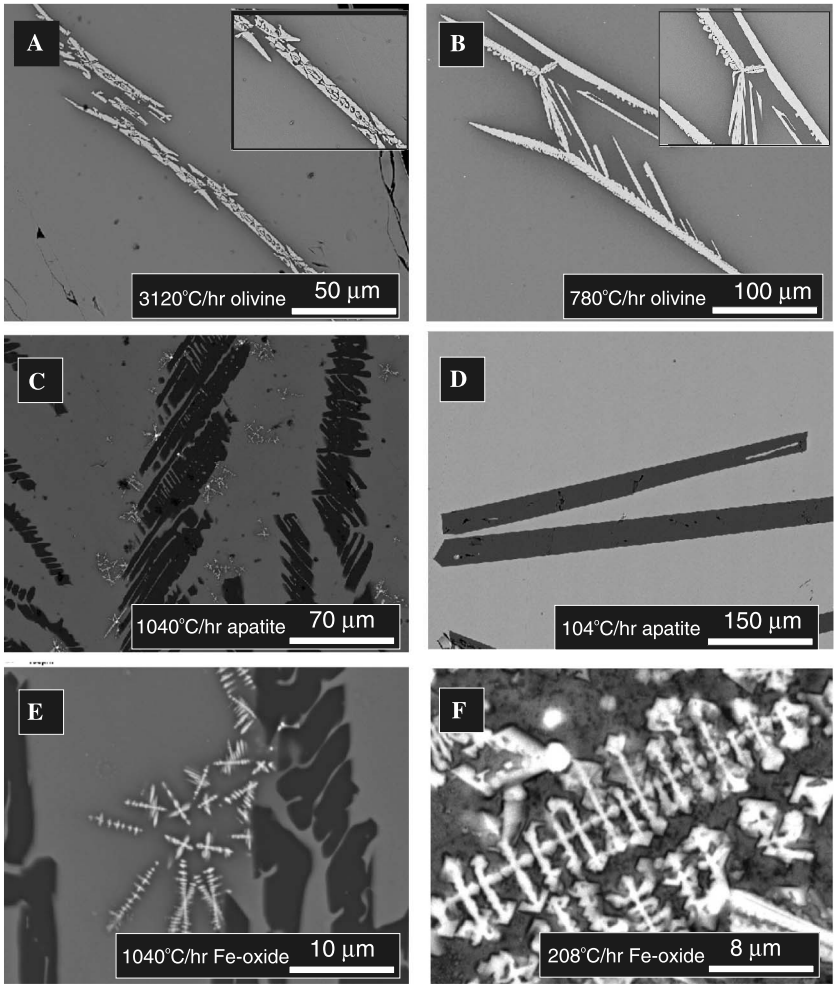

Fig. 6. SEM BSE photomicrographs showing the change in crystal shape with decreasing cooling rate (see caption box at the bottom of each image). (A and B) are from melt pocket 1 and melt pocket 4 (C–F). The boxes in the upper right hand corner of (A and B) show a higher magnification image. Images on the right side show change in crystal shape as cooling rate decreases (B, D, and F). This is most obvious for the apatite dendrite shown in (C–D). At a cooling rate of 104 °C/h the crystal shape becomes polyhedral with well-defined faces. The polyhedral crystals typically contain spherical or elongate melt inclusions. All photomicrographs are of textures observed in experimental runs.

melt pocket crystals to indicate good fits. LA 001 melt pocket 1 and 4 cooling rates overlap at 1040–1560 °C/h (8–12 min duration). Melt pocket 5, representative of DaG 476 and SaU 150, cooled at 780 °C/h (16 min duration).

6.3. Cooling rates: experimental versus theory

Heat conduction models, solved for a range of meteoroid diameters (10–100 cm), show that a melt pocket located at the meteoroid center, ~5 cm from the meteoroid surface would cool over a time period of minutes (~24–30 min). With increasing meteoroid diameter (25–50 cm) the melt pockets would remain fluid for hours. At the upper limit (100 cm) the melt pockets would take approximately one day, to at most a few days, to cool. Comparing the model calculations to the experimental results, the conductive cooling models predict a minimum meteoroid diameter at the decimeter scale, $\leqslant$10 cm. At this diameter a melt pocket would cool within minutes, consistent with dynamic crystallization of LA 001 melt pockets 1 and 4 (8–12 min), and DaG 476/SaU 150 (16 min). The heat conduction model calculations also show a good fit with previous size estimates for rock fragments ejected from impact craters (0.1–50 cm diameter; Pohl et al., 1977; Stöffler and Ostertag, 1983; Ceplecha et al., 1993; Eugster et al., 2002; Bland and Artemieva, 2003; Artemieva and Ivanov, 2004).

The conductive cooling models only constrain the minimum meteoroid diameter. In the model, we assume that the melt pockets were located in the center of the meteoroid. However, they could have been located at any depth between the meteoroid center and its surface. Indeed, this is the case for SaU 150 which is one of ten paired meteorites encompassing 17 specimens having a combined mass of ~11 kg. Assuming a density of 3.23 g/cm^3 (appropriate for basalt) this corresponds to a diameter of ~19 cm. Although only placing a minimum estimate on meteoroid diameter, the model is significant in that it is consistent with launch of small rock fragments during impact.

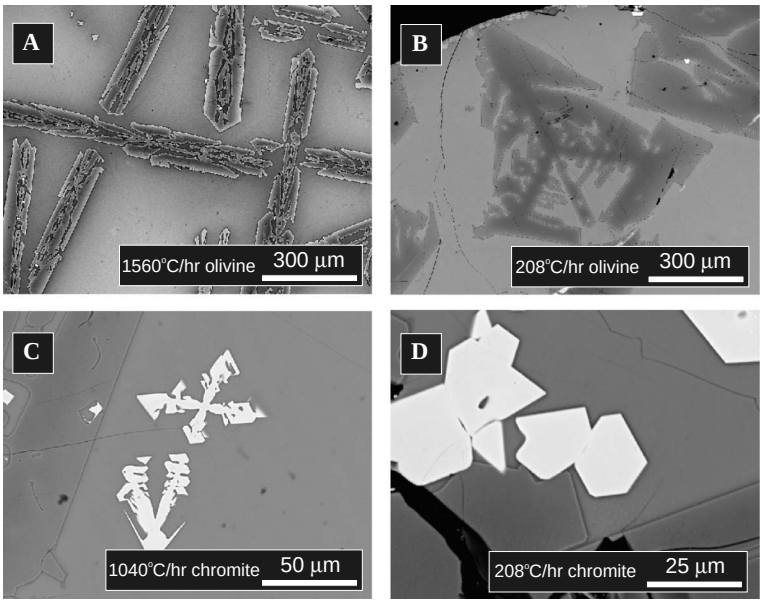

Fig. 7. SEM BSE photomicrographs of melt pocket 5 showing the change in crystal morphology as cooling rate decreases (see caption box at the bottom of each image). (A) Swallowtail crystals formed at a cooling rate of 1560 °C/h progress to skeletal shapes at lower cooling rates (108 °C/h) (B). (C) Dendritic chromite (1040 °C/h). (D) Polyhedral chromite formed at a cooling rate of 208 °C/h containing spherical melt inclusions. All photomicrographs are of crystals observed in experimental runs.

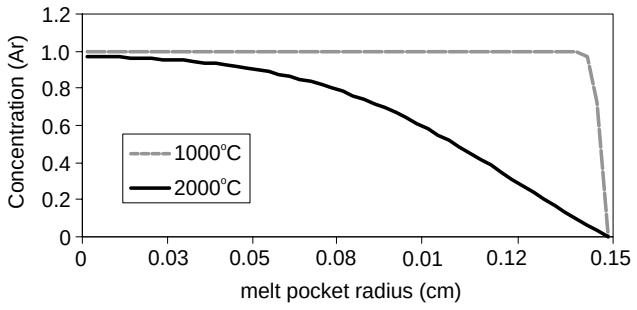

Fig. 8. Argon loss from a melt pocket of radius 0.15 cm at 1000 and 2000 °C. At the lower temperature limit ~4% of argon is lost from the system. At the upper temperature limit melt pocket loss reaches ~60%.

6.4. Melt pocket formation

The results of this study describe the post-shock cooling history of melt pockets. Although the melt pocket cooling history does not relate directly to formation mechanisms, they do have bearing on trapped martian atmosphere because it is during the liquid stage of melt pocket evolution that the atmosphere becomes trapped in the melt pockets and during cooling that melt pockets have the potential to lose gases.

Using the experimentally determined diffusivity of argon measured in synthetic glasses of albite ($NaAlSi_3O_8$) composition (Carroll, 1991), and equations solving non-steady state diffusion in a sphere (Crank, 1975), we have estimated the amount of argon loss from the melt pocket to surrounding minerals.

Variations in the Ar diffusion coefficient (D) with temperature, can be described by the Arrhenius relationship:

$$D = D_0 * \exp^{(-E/RT)},$$

where D_0 (Ab) $= 1.62 \times 10^{-3}$ cm^2/s, $E = 1.372 \times 10^5$ J/mol, $R = 8.3144$ J/mol/K and $T =$ temperature in Kelvin. By using a maximum temperature of 2300 K (2027 °C; assuming superheating of the melt pockets during shock melting) and a lower temperature limit of 1273 K (1000 °C; lowest temperature reached during the experiments), we calculate $D = 1.24 \times 10^{-6}$ cm^2/s (2000 K) and $D = 3.82 \times 10^{-9}$ cm^2/s (1273 K).

The total amount of diffusing substance (argon) entering or leaving the sphere can be solved by

$$C_{\mathrm{m}} := \frac{2 \cdot a}{\pi \cdot r_{\mathrm{m}}} \cdot \left[\sum_n \frac{(-1)^n}{n} \cdot \sin\left(\left(\frac{n \cdot \pi \cdot r_m}{a} \right) \right) \cdot \left[\mathrm{e}^{\left(\frac{-D \cdot n^2 \cdot \pi^2 \cdot t}{a^2} \right)} \right] \right] \cdot -1,$$

where C_{m} is the concentration of diffusing substance, a is the radius of the sphere, and t is the time in seconds. We have chosen a melt pocket (sphere) radius of 0.15 cm and calculated temperature-dependent argon loss over 16 min (960 s; the maximum cooling duration determined by the crystallization experiments). For an upper T limit of 2300 K, 60% of argon would be lost through diffusive transport (Fig. 8). At the lower T limit (1200 K) only 4% of the argon is lost (Fig. 8). It is likely that the actual amount of argon lies between these limits, probably 20–30%. Since diffusion is a non-fractionating process, the

amounts of argon lost will not affect recognition of a trapped martian atmospheric component (i.e., $^{40}Ar/^{36}Ar$ ratio; Garrison and Bogard, 1998). However, the total amount of argon will be affected.

7. Conclusion

The experiments performed to grow quench crystals from three distinct starting compositions at various cooling rates over a constant cooling interval constrain the time that the melt pockets remained fluid after shock pressure release, and the minimum meteoroid diameter. Qualitative and quantitative analysis of melt pocket textures and mineralogy show the best fit for a cooling duration of 12–16 min. Using conductive cooling models, the dataset indicates that the original (pre-atmospheric) meteoroid diameter was small, on the order of 10–15 cm and that cooling occurred within minutes. The results of conductive cooling models and estimates for minimum meteoroid diameter are compatible with the experimentally determined cooling rates. This implies that the experiment provides a reasonable method for estimating cooling rates and that fractal analysis of crystal shapes is useful for constraining cooling rate when runs cooled at different rates show similar shapes. During cooling ~4–60% of martian atmospheric argon can be lost from the melt pocket through diffusive transport.

Acknowledgments

This work has been funded through NSERC and CSA grants to E.W., and NSERC grants to C.S. and J.S. We thank Tony Fowler, Gary Lofgren, and David Mittlefehldt for their reviews of an earlier version of this manuscript. Planetary and Space Science Centre contribution 45.

Associate editor: David W. Mittlefehldt

References

Artemieva, N., Ivanov, B., 2004. Launch of martian meteorites in oblique impacts. *Icarus* **171**, 84–101.

Asimow, P.D., Ghiorso, M.S., 1998. Algorithmic modifications extending MELTS to calculate subsolidus phase relations. *Am. Miner.* **83**, 1127–1132.

Avnir, D., 1989. *The Fractal Approach to Heterogeneous Chemistry, Surfaces, Colloids, Polymers*. John Wiley, Chichester.

Beck, P., Gillet, P., Gautron, L., Daniel, I., El Goresy, A., 2004. A new natural high-pressure (Na,Ca)-hexaluminosilicate $[(Ca_xNa_{1-x})Al_{3+x}Si_{3-x}O_{11}]$ in shocked Martian meteorites. *Earth Planet. Sci. Lett.* **219**, 1–12.

Bland, P.A., Artemieva, N.A., 2003. Efficient disruption of small asteroids by Earth's atmosphere. *Nature* **424**, 288–291.

Bogard, D.D., Johnson, P., 1983. Martian gases in an Antarctic meteorite? *Science* **221**, 651–654.

Bogard, D.D., Hörz, F., Johnson, P., 1989. Shock-implanted noble gases II: additional experimental studies and recognition in naturally shocked terrestrial materials. *Meteoritics* **24**, 113–123.

Carroll, M.R., 1991. Diffusion of Ar in rhyolite, orthoclase and albite composition glasses. *Earth Planet. Sci. Lett.* **103**, 156–168.

Carslaw, H.S., Jaeger, J.C., 1959. *Conduction of Heat in Solids*. Clarendon Press, Oxford.

Ceplecha, Z., Spurný, P., Borovička, J., Keclíková, J., 1993. Atmospheric fragmentation of meteoroids. *Astron. Astrophys.* **279**, 615–626.

Crank, J., 1975. *The Mathematics of Diffusion*. Clarendon Press, Oxford.

Donaldson, C.H., 1976. An experimental investigation of olivine morphology. *Contrib. Mineral. Petrol.* **57**, 187–213.

Dressler B.O., Sharpton V.L. (1998) Coexisting pseudotachylite and rock glasses at the Haughton impact crater, Canada. *Lunar Planet. Sci. XXXI*. Lunar Planet Inst., Houston. #1384 (abstract).

Eugster, O., Busemann, H., Lorenzetti, S., Terribilini, D., 2002. Ejection ages from ^{81}Kr–^{83}Kr dating and pre-atmospheric sizes of Martian meteorites. *Meteor. Planet. Sci.* **37**, 1345–1360.

Faure, F., Trolliard, G., Nicollet, C., Montel, J.-M., 2003. A developmental model of olivine morphology as a function of the cooling rate and the degree of undercooling. *Cryst. Growth Melt* **145**, 251–263.

Fowler, A.D., 1995. Mineral crystallinity in igneous rocks: fractal method. In: Barton, C.C., La Point, P.R. (Eds.), *Fractals in the Earth Science*. Plenum Press, New York, pp. 237–249.

Fowler, A.D., Stanley, H.E., Daccord, G., 1989. Disequilibrium silicate mineral textures: fractal and non-fractal features. *Nature* **341**, 134–138.

Fritz, J., Greshake, A., Stöffler, D., 2003. Launch conditions for Martian meteorites: plagioclase as a shock pressure barometer. *Lunar Planet. Sci. XXXIV*. Lunar Planet. Inst., Houston. #1335 (abstract).

Garrison, D.H., Bogard, D.D., 1998. Isotopic composition of trapped and cosmogenic noble gases in several martian meteorites. *Meteor. Planet. Sci.* **33**, 721–736.

Ghiorso, M.S., Sack, R.O., 1995. Chemical mass transfer in magmatic processes' IV, A revised and internally consistent thermodynamic model for interpolation and extrapolation of liquid–solid equilibria in magmatic systems at elevated temperatures and pressures. *Contrib. Mineral. Petrol.* **119**, 197–212.

Gladman, B., 1997. Destination Earth: Martian meteorite delivery. *Icarus* **130**, 228–246.

Gnos, E., Hofmann, B., Franchi, I.A., Al-Kathiri, A., Hauser, M., Moser, L., 2002. Sayh al Uhaymir 094: a new martian meteorite from the Oman desert. *Meteor. Planet. Sci.* **37**, 835–854.

Huebner, J.S., 1971. Buffering techniques for hydrostatic systems at elevated pressures. In: Ulmer, G.C. (Ed.), *Research Techniques for High Pressure and High Temperature*. Springer-Verlag, Berlin, pp. 123–177.

Ivanov, B.A., Deutsch, A., 1999. Sudbury impact event: Cratering mechanics and thermal history. In: Dressler, B.O., Sharpton, V.L., (Eds.), *Large Meteorite Impacts and Planetary Evolution II. Geol. Soc. Amer. Spec. Paper*. 339. Boulder, Colorado. pp. 389–397.

Lofgren, G., 1980. Experimental studies on the dynamic crystallization of silicate melts. In: Hargraves, R.B. (Ed.), *Physics of Magmatic Processes*. Princeton University Press, New Jersey, pp. 487–551.

Mandelbrot, B.B., 1982. *The Fractal Geometry of Nature*. W.H. Freeman, New York.

Ostertag, R., Robertson, P.B., Stöffler, D., Wöhr-Meyer, C., 1984. First results of a multidisciplinary analysis of the Haugton impact crater, Devon Island, Canada III. Petrography and shock metamorphism. *Lunar Planet. Sci. XVI*. Lunar Planet. Inst., Houston. 633–634 (abstract).

Pohl, J., Stöffler, D., Gall, H., Ernston, K., 1977. The Ries impact crater. In: Roddy, D.H., Pepin, R.O., Merill, R.B. (Eds.), *Impact and Explosion Cratering*. Pergamon Press, New York, pp. 343–404.

Raikhlin, A.I., Danilin, A.N., Kozlov, V.S., Reshetnyak, N.B., 1981. Chilling products of superheated impact melts from some astroblemes of the U.S.S.R. territory. *Lunar Planet. Sci. XII*. Lunar Planet. Inst., Houston. 860–862 (abstract).

Schmitt, R.T., 2000. Shock experiments with the H6 chondrite Kernouvé: pressure calibration of microscopic shock effects. *Meteor. Planet. Sci.* **35**, 545–560.

Spray, J.G., Rae, D.A., 1995. Quantitative electron-microprobe analysis of alkali silicate glasses: a review and user guide. *Can. Mineral.* **33**, 323–332.

Stöffler, D., Ostertag, R., 1983. The Ries impact crater. *Fortschr. Mineral.* **61**, 71–116.

Stöffler, D., Knöll, H.-D., Maerz, U., 1979. Terrestrial and lunar impact breccias and the classification of lunar highland rocks. *Proc. Lunar Planet. Sci. Conf.* **10**, 639–675.

Stöffler, D., Ostertag, R., Jammes, C., Pfannschmidt, G., Sen Gupta, P.R., Simon, S.B., Papike, J.J., Beauchamp, R.H., 1986. Shock metamorphism and petrography of the Shergotty achondrite. *Geochim. Cosmochim. Acta* **50**, 889–903.

Stöffler, D., Keil, K., Scott, E.R.D., 1991. Shock metamorphism of ordinary chondrites. *Geochim. Cosmochim. Acta* **55**, 3845–3867.

Walton, E.L., Spray, J.G., 2003. Mineralogy, microtexture, and composition of shock-induced melt pockets in the Los Angeles basaltic shergottite. *Meteor. Planet. Sci.* **38**, 1865–1875.

Wiens, R.C., Pepin, R.O., 1988. Laboratory shock emplacement of noble gases, nitrogen, and carbon dioxide into basalt, and implications for trapped gases in shergottites EETA 79001. *Geochim. Cosmochim. Acta* **52**, 295–307.

Zombeck, M.V., 1990. *Handbook of Space Astronomy and Astrophysics*. Cambridge University Press, New York.

Zurek, R.W., Barnes, J.R., Haberle, R.M., Pollack, J.B., Tillman, J.E., Levoy, C.B., 1992. Dynamics of the atmosphere of Mars. In: Kieffer, H.H., Jakowsky, B.M., Synder, C.W., Mathews, M.S. (Eds.), *Mars*. University of Arizona Press, Tucson, pp. 835–933.